

# Chiral extrapolations for nucleon electric charge radii

J. M. M. Hall,<sup>1</sup> D. B. Leinweber,<sup>1</sup> and R. D. Young<sup>1,2</sup>

<sup>1</sup>*Special Research Centre for the Subatomic Structure of Matter (CSSM),*

*School of Chemistry and Physics, University of Adelaide, Adelaide, South Australia 5005, Australia*

<sup>2</sup>*ARC Centre of Excellence for Particle Physics at the Terascale, School of Chemistry and Physics, University of Adelaide, Adelaide, South Australia 5005, Australia*

Lattice simulations for the electromagnetic form factors of the nucleon yield insights into the internal structure of hadrons. The logarithmic divergence of the charge radius in the chiral limit poses an interesting challenge in achieving reliable predictions from finite-volume lattice simulations. Recent results near the physical pion mass ( $m_\pi \sim 180$  MeV) are examined in order to confront the issue of how the chiral regime is approached. The electric charge radius of the nucleon isovector presents a forum for achieving consistent finite-volume corrections. Newly developed techniques within the framework of chiral effective field theory ( $\chi$ EFT) are used to achieve a robust extrapolation of the electric charge radius to the physical pion mass, and to infinite volume. The chiral extrapolations exhibit considerable finite-volume dependence; lattice box sizes of  $L \gtrsim 7$  fm are required in order to achieve a direct lattice simulation result within 2% of the infinite-volume value at the physical point. Predictions of the volume dependence are provided to guide the interpretation of future lattice results.

PACS numbers: 12.38.Gc 12.38.Aw 12.39.Fe 13.40.Em

## I. INTRODUCTION

Much experimental progress has been made [1–5] in examining the internal structure of hadrons, particularly with regard to the internal distribution of electric and magnetic charge due to quarks. Current understanding of the internal charge distribution, characterized by the elastic form factors, is also fortified by developments in supercomputing power and lattice QCD techniques. Lattice QCD has seen significant advances in simulating electromagnetic form factors, and is now able to probe the chiral regime [6–9].

Recent results from the QCDSF Collaboration, using pion masses of order  $\sim 180$  MeV [10], provide a new opportunity for exploring the utility of chiral effective field theory ( $\chi$ EFT)-based techniques in performing an extrapolation to the physical point. Additional care must be taken in handling finite-volume effects relating to the electric charge radius [11–14]. In order to address this issue, a variety of *Ansätze* for the  $Q^2$  behaviour of the form factor are examined in order to construct a finite-volume analogue. The finite-volume corrections are applied directly to the electric form factors, and the electric charge radii are then calculated at infinite volume. By combining these methods with new techniques within the framework of  $\chi$ EFT, a robust extrapolation to the physical regime is performed herein.

In performing a chiral extrapolation, one should ideally use lattice simulation results that lie within the chiral power-counting regime (PCR) of chiral perturbation theory in order to avoid a regularization scheme-dependent result. The PCR is defined by the range of quark (or pion) masses at which a  $\chi$ EFT calculation is independent of the regularization scheme, and typically lies in a pion-mass range of  $\lesssim 200$  MeV [15–17]. Within the PCR, the chiral expansion of an observable is a controlled expansion, and the result is insensitive to treatments of higher-order terms, such as the resummation of the chiral series. Since lattice QCD results usually extend outside the PCR, one is restricted by the available data when per-

forming an extrapolation. An important application of finite-range regularization (FRR) is the ability to extrapolate using lattice QCD results that extend beyond the PCR. One method for achieving this involves identifying a preferred regularization scale and an upper bound of the pion mass directly from the lattice QCD results, as demonstrated in Refs. [18, 19]. In a previous investigation, a successful extrapolation of the magnetic moment of the nucleon to the physical point was achieved using these techniques [20]. This analysis similarly provides a prediction of the pion-mass dependence of the electric charge radius of the nucleon for a range of lattice volumes.

The lattice QCD results from the QCDSF Collaboration [10] used in this analysis are displayed in Fig. 1. The simulation used a two-flavor  $\mathcal{O}(a)$ -improved Wilson quark action, and the isovector nucleon ( $p - n$ ) was calculated to avoid the computational cost of disconnected loops that occur in full QCD. Only the simulation results that satisfy the criteria:  $L > 1.5$  fm and  $m_\pi L > 3$ , are shown. Of the nine points that satisfy these criteria, the lattice size varies from 1.7 to 2.9 fm. The QCDSF results are displayed using a Sommer scale parameter of  $r_0 = 0.475$  fm, based on results from Ref. [21]. Without consideration of chiral loop contributions, it is clear that there would be a factor of two discrepancy between the lattice QCD simulations and the experimental value [22, 23] as shown by a linear trend line.

## II. CHIRAL EFFECTIVE FIELD THEORY

### A. Electromagnetic form factors

It is common to define the Sachs electromagnetic form factors  $G_{E,M}$ , which parametrize the matrix element for the quark current  $J_\mu$ . In the heavy-baryon limit, this can be writ-

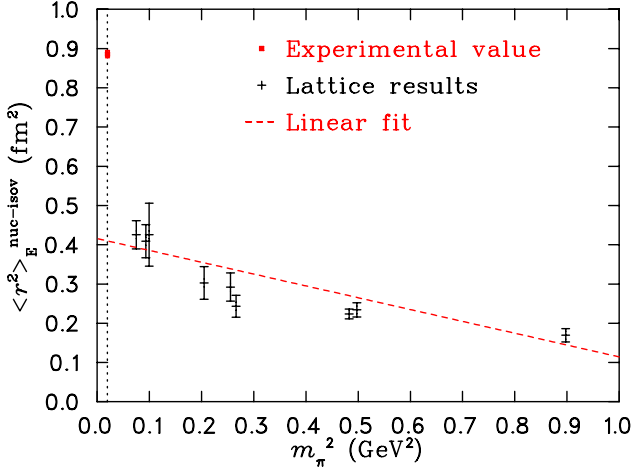


FIG. 1: (color online). Lattice QCD results for  $\langle r^2 \rangle_E$  from QCDSF [10], using the Ansatz from Eq. (31), and the experimental value as marked [22, 23]. The lattice results satisfy:  $L > 1.5$  fm and  $m_\pi L > 3$ . A naïve linear trend line is also included, which does not reach the experimental value. The physical point is shown with a vertical dotted line.

ten as

$$\langle B(p') | J_\mu | B(p) \rangle = \bar{u}^{s'}(p') \left\{ v_\mu G_E(Q^2) + \frac{i\epsilon_{\mu\nu\rho\sigma} v^\rho S_\nu^\sigma q^\nu}{m_B} G_M(Q^2) \right\} u^s(p), \quad (1)$$

where  $Q^2$  is defined as positive momentum transfer  $Q^2 = -q^2 = -(p' - p)^2$ . Lattice QCD results are often constructed from an alternative representation, using the form factors  $F_1$  and  $F_2$ , the Dirac and Pauli form factors, respectively. The Sachs form factors are simply linear combinations of  $F_1$  and  $F_2$ ,

$$G_E(Q^2) = F_1(Q^2) - \frac{Q^2}{4m_B^2} F_2(Q^2), \quad (2)$$

$$G_M(Q^2) = F_1(Q^2) + F_2(Q^2). \quad (3)$$

In the heavy-baryon formulation of the quark current matrix element shown in Eq. (1), the spin operator  $S_\nu^\mu = -\frac{1}{4}\gamma_5[\gamma^\mu, \gamma^\nu]v_\nu$  is required. It has the useful properties in that its commutation and anticommutation rules depend only on the four-velocity of the baryon  $v_\mu$  [24, 25]. The momentum-dependent electric form factor  $G_E(Q^2)$  allows a charge radius to be defined in the usual manner,

$$\langle r^2 \rangle_E = \lim_{Q^2 \rightarrow 0} -6 \frac{\partial G_E(Q^2)}{\partial Q^2}. \quad (4)$$

For the leading-order contributions to the electric form factor, the following first-order interaction Lagrangian from heavy-baryon chiral perturbation theory ( $\chi$ PT) is used [24–29],

$$\mathcal{L}_{\chi PT}^{(1)} = 2D \text{Tr} [\bar{B}_\nu S_\nu^\mu \{A_\mu, B_\nu\}] + 2F \text{Tr} [\bar{B}_\nu S_\nu^\mu [A_\mu, B_\nu]] + C (\bar{T}_\nu^\mu A_\mu B_\nu + \bar{B}_\nu A_\mu T_\nu^\mu). \quad (5)$$

The pseudo-Goldstone fields  $\xi(x)$  are encoded in the adjoint representation of  $SU(3)_L \otimes SU(3)_R$ , forming an axial vector

combination, denoted  $A_\mu$ ,

$$\xi \equiv \exp \left\{ \frac{i}{f_\pi} \tau^a \pi^a \right\}, \quad (6)$$

$$A_\mu = \frac{1}{2} (\xi \partial_\mu \xi^\dagger - \xi^\dagger \partial_\mu \xi). \quad (7)$$

The values for the  $D$ ,  $F$  and  $C$  couplings in the interaction Lagrangian are related through  $SU(6)$  flavor-symmetry [25, 30],  $F = \frac{2}{3}D$  and  $C = -2D$ . Phenomenological values of the constants  $D = 0.76$  and  $f_\pi = 92.4$  MeV are used.

## B. Finite-range regularization

In FRR  $\chi$ EFT, a regulator function  $u(k; \Lambda)$ , with characteristic momentum scale  $\Lambda$ , is introduced in the numerators of the loop integrals. The regulators should be chosen such that they satisfy  $u|_{k=0} = 1$  and  $u|_{k \rightarrow \infty} = 0$ . The result of an FRR calculation is independent of the choice of  $u(k; \Lambda)$  if the lattice simulation points are constrained entirely within the PCR. In this investigation, a dipole form is chosen, which takes the following form,

$$u(k; \Lambda) = \left( 1 + \frac{k^2}{\Lambda^2} \right)^{-2}. \quad (8)$$

While conventional  $\chi$ PT fails outside the PCR, FRR  $\chi$ EFT remains effective, as the regulator takes on an additional role in modelling the effect of higher-order terms in the expansion. Analyses have been undertaken previously for a range of possible forms of regulator function [17, 18].

## C. Loop integrals and definitions

The leading-order loop integral contributions to the electric form factor correspond to the diagrams in Figs. 2 through 4. The electric charge radius itself is also renormalized by contributions from loop integrals, obtained from  $\chi$ EFT. The loop integrals can be simplified to a convenient form by taking the heavy-baryon limit, and performing the pole integrations for  $k_0$ ,

$$\mathcal{T}_N^E(Q^2) = -\frac{\chi_N^E}{5\pi} \int d^3k \frac{(k^2 - \vec{k} \cdot \vec{q}) u(\vec{k}; \Lambda) u(\vec{k} - \vec{q}; \Lambda)}{\omega_{\vec{k}} \omega_{\vec{k} - \vec{q}} (\omega_{\vec{k}} + \omega_{\vec{k} - \vec{q}})}, \quad (9)$$

$$\mathcal{T}_\Delta^E(Q^2) = -\frac{\chi_\Delta^E}{5\pi} \int d^3k \frac{(k^2 - \vec{k} \cdot \vec{q}) u(\vec{k}; \Lambda) u(\vec{k} - \vec{q}; \Lambda)}{(\omega_{\vec{k}} + \Delta) (\omega_{\vec{k} - \vec{q}} + \Delta) (\omega_{\vec{k}} + \omega_{\vec{k} - \vec{q}})}, \quad (10)$$

$$\mathcal{T}_{\text{tad}}^E(Q^2) = -\frac{\chi_t^E}{\pi} \int d^3k \frac{u^2(\vec{k}; \Lambda)}{\omega_{\vec{k}} + \omega_{\vec{k} - \vec{q}}}, \quad (11)$$

where  $\omega_{\vec{k}} = \sqrt{\vec{k}^2 + m_\pi^2}$  and  $\Delta$  is the baryon mass splitting.

The coefficients  $\chi_N^E$ ,  $\chi_\Delta^E$  and  $\chi_t^E$ , for both proton ( $p$ ) and neutron ( $n$ ), are related to the constants  $D$ ,  $F$ ,  $C$  and  $f_\pi$  from

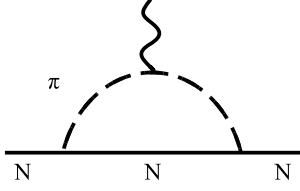


FIG. 2: The pion loop contributions to the electric charge radius of a nucleon. All charge conserving pion-nucleon transitions are implicit.

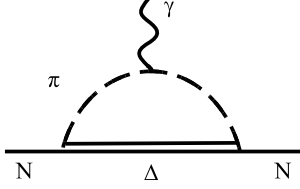


FIG. 3: The pion loop contribution to the electric charge radius of a nucleon, allowing transitions to the nearby and strongly-coupled  $\Delta$  baryons.

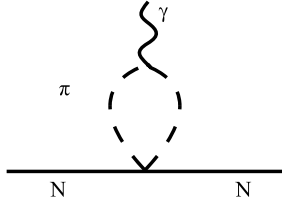


FIG. 4: The tadpole contribution at  $\mathcal{O}(m_q)$  to the electric charge radius of a nucleon.

the chiral Lagrangian in Eq. (5),

$$\chi_N^{E,p} = -\frac{5}{16\pi^2 f_\pi^2} (D + F)^2 = -\chi_N^{E,n}, \quad (12)$$

$$\chi_\Delta^{E,p} = +\frac{5}{16\pi^2 f_\pi^2} \frac{4C^2}{9} = -\chi_\Delta^{E,n}, \quad (13)$$

$$\chi_t^{E,p} = -\frac{1}{16\pi^2 f_\pi^2} = -\chi_t^{E,n}. \quad (14)$$

#### D. Finite-volume corrections

Finite-volume corrections cannot be applied directly to the charge radius itself [14]. Instead, the electric form factors  $G_E(Q^2)$  are corrected to infinite-volume. To obtain the integrals  $T^E$  that contribute to the electric charge radius, one takes the derivative of  $\mathcal{T}^E$  with respect to momentum transfer  $\vec{q}^2$ , as  $\vec{q}^2 \rightarrow 0$ ,

$$T^E = \lim_{\vec{q}^2 \rightarrow 0} -6 \frac{\partial \mathcal{T}^E(\vec{q}^2)}{\partial \vec{q}^2}, \quad (15)$$

which is equivalent to the derivative in Eq. (4) in the Breit frame, defined by  $q = (0, \vec{q})$ .

The finite-volume corrections to the electric form factors

are achieved by subtracting the electric charge symmetry-preserving finite-volume correction, defined as

$$\Delta_L(Q^2, 0) = \delta_L[\mathcal{T}^E(Q^2)] - \delta_L[\mathcal{T}^E(0)]. \quad (16)$$

The functional  $\delta_L$  is defined through the convention [31]:

$$\delta_L[\mathcal{T}^E(Q^2)] = \chi \left[ \frac{(2\pi)^3}{L_x L_y L_z} \sum_{k_x, k_y, k_z} - \int d^3k \right] \mathcal{I}^E(Q^2), \quad (17)$$

for an integrand  $\mathcal{I}^E$ . The second term of Eq. (16) ensures that both infinite- and finite-volume electric form factors are correctly normalized, i.e.  $G_E(0) = 1$ . This normalization procedure exploits the lattice Ward Identity that ensures charge conservation is satisfied in a finite volume. It has been shown previously that this is realised in practice; numerically and through  $\chi$ EFT analyses [14]. Thus, the infinite-volume electric form factor can be calculated using the equation:

$$G_E^\infty(Q^2) = G_E^L(Q^2) - \Delta_L(Q^2, 0). \quad (18)$$

The infinite-volume charge radius  $\langle r^2 \rangle_E^\infty$  can be recovered from the form factor by choosing an *Ansatz* for the extrapolation in  $Q^2$ , analogous to the procedure typically performed at finite volume.

In applying FRR to the finite-volume corrections, the value of  $\Delta_L(Q^2, 0)$  stabilises as  $\Lambda$  becomes large. Applying the same technique as in Ref [18], the asymptotic result of  $\Delta_L(Q^2, 0)$  is achieved numerically by evaluating it with a dipole regulator, using a relatively large value of  $\Lambda' = 2.0$  GeV. This method is similar to the algebraic approach outlined in Ref. [32], and has been successfully demonstrated in previous studies [33].

#### E. Renormalization

The procedure for the renormalization of the low-energy coefficients of the chiral expansion in FRR  $\chi$ EFT will now be outlined. A thorough discussion can be found in Ref. [18].

Each loop integral contributing to the electric charge radius may be expanded out as an analytic polynomial plus a non-analytic term,

$$T_N^E(m_\pi^2; \Lambda) = b_0^{\Lambda, N} + \chi_N^E \log \frac{m_\pi}{\mu} + b_2^{\Lambda, N} m_\pi^2 + \mathcal{O}(m_\pi^4), \quad (19)$$

$$T_\Delta^E(m_\pi^2; \Lambda) = b_0^{\Lambda, \Delta} + b_2^{\Lambda, \Delta} m_\pi^2 + \frac{\chi_\Delta^E}{2\Delta^2} m_\pi^2 \log \frac{m_\pi}{\mu} + \mathcal{O}(m_\pi^4), \quad (20)$$

$$T_{\text{tad}}^E(m_\pi^2; \Lambda) = b_0^{\Lambda, t} + \chi_t^E \log \frac{m_\pi}{\mu} + b_2^{\Lambda, t} m_\pi^2 + \mathcal{O}(m_\pi^4), \quad (21)$$

where  $\mu$  is a mass scale associated with the chiral logarithm. Once the lattice results have been converted into infinite-volume charge radii, the chiral behaviour of the electric charge

radius can be written in terms of an ordered expansion in pion-mass squared, through use of the Gell-Mann–Oakes–Renner Relation,  $m_q \propto m_\pi^2$  [34],

$$\langle r^2 \rangle_E^\infty = \{a_0^\Lambda + a_2^\Lambda m_\pi^2\} + T_N^E(m_\pi^2; \Lambda) + T_\Delta^E(m_\pi^2; \Lambda) + T_{\text{tad}}^E(m_\pi^2; \Lambda) + \mathcal{O}(m_\pi^4). \quad (22)$$

This expansion contains an analytic polynomial in  $m_\pi^2$  plus the leading-order chiral loop integrals, from which nonanalytic behaviour arises. The scale-dependent coefficients  $a_i^\Lambda$  are the residual series coefficients, which correspond to direct quark-mass insertions in the full Lagrangian. Upon renormalization of the divergent loop integrals, these will correspond with low-energy coefficients of  $\chi\text{EFT}$  [35].

In order to obtain the renormalized chiral coefficients,  $c_i$ , one must add the  $b_i^\Lambda$  terms from each of the loop integrals to the residual series coefficients  $a_i^\Lambda$ ,

$$c_0 = a_0^\Lambda + b_0^{\Lambda, N} + b_0^{\Lambda, \Delta} + b_0^{\Lambda, t}, \quad (23)$$

$$c_2 = a_2^\Lambda + b_2^{\Lambda, N} + b_2^{\Lambda, \Delta} + b_2^{\Lambda, t}. \quad (24)$$

The resultant coefficients,  $c_0$  and  $c_2$ , are the renormalized low-energy coefficients of the chiral expansion at the scale,  $\mu$ . By evaluating the loop integrals, the renormalized chiral expansion can also be written in terms of a polynomial in  $m_\pi^2$  and the nonanalytic terms,

$$\langle r^2 \rangle_E^\infty = c_0^{(\mu)} + (\chi_N^E + \chi_t^E) \log \frac{m_\pi}{\mu} + c_2 m_\pi^2 + \frac{\chi_\Delta^E}{2\Delta^2} m_\pi^2 \log \frac{m_\pi}{\mu} + \mathcal{O}(m_\pi^4), \quad (25)$$

reproducing  $\chi\text{PT}$  in the PCR. Since the chiral expansion of Eq. (25) contains a logarithm, the value of  $c_0$  can only be extracted relative to the mass scale,  $\mu$ , which is chosen to be 1 GeV in this case.

To achieve a chiral extrapolation, it is convenient to subtract the  $b_0^\Lambda$  coefficients from the respective loop integrals, thus automating the renormalization procedure to chiral order  $\mathcal{O}(1)$ ,

$$\tilde{T}_N^E = T_N^E - b_0^{\Lambda, N}, \quad (26)$$

$$\tilde{T}_\Delta^E = T_\Delta^E - b_0^{\Lambda, \Delta}, \quad (27)$$

$$\tilde{T}_{\text{tad}}^E = T_{\text{tad}}^E - b_0^{\Lambda, t}. \quad (28)$$

This removes the dependence on the regularization scale  $\Lambda$  in the leading low-energy coefficient. Thus, the chiral formula used for fitting lattice QCD results takes the form:

$$\langle r^2 \rangle_E^\infty = \{c_0^{(\mu)} + a_2^\Lambda m_\pi^2\} + \tilde{T}_N^E + \tilde{T}_\Delta^E + \tilde{T}_{\text{tad}}^E + \mathcal{O}(m_\pi^4). \quad (29)$$

To ascertain the presence of an optimal regularization scale  $\Lambda^{\text{scale}}$ , the renormalization flow of the leading low-energy coefficient  $c_0^{(\mu)}$  will be considered in Sec. III B, using the prescription detailed in Refs. [18–20].

### III. RESULTS

#### A. $Q^2$ extrapolation

In extracting an electric charge radius from typical lattice QCD results on periodic volumes, one must choose an *Ansatz* to model the finite-volume corrected  $Q^2$  behaviour of the electric form factor. A common choice is the dipole form, defined by

$$G_E(Q^2) = \frac{G_E(0)}{(1 + Q^2/\Lambda_D^2)^2}, \quad (30)$$

where the dipole mass  $\Lambda_D$  is a free parameter, related to the electric charge radius by  $\Lambda_D^2 = 12/\langle r^2 \rangle_E$ . This *Ansatz* tightly constrains the  $Q^2$  dependence and leads to small errors in the radius  $\langle r^2 \rangle_E$  compared with other *Ansätze*. These dipole-constrained radii are shown in Fig. 5.

A modification may be made to account for higher order terms in  $Q^2$ . An inverse quadratic with two fit parameters, as inspired by Kelly [36], may be chosen. This form is used in the analysis by the QCDSF Collaboration [10],

$$G_E(Q^2) = \frac{G_E(0)}{1 + \alpha Q^2 + \beta Q^4}. \quad (31)$$

The charge radius is obtained through  $\langle r^2 \rangle_E = 6\alpha$ . This *Ansatz* was originally chosen for modelling the large  $Q^2$  behaviour of  $F_1$  [10, 36]. However, it is of greater interest here to examine and compare the *small*  $Q^2$  behaviour of this *Ansatz* with that of the dipole. Furthermore, this will provide a guide to the expected variation in  $\langle r^2 \rangle_E$  due to the choice of *Ansatz*.

A demonstration of an infinite-volume chiral extrapolation using each *Ansatz* is shown in Figs. 5 and 6. In each case, the smallest three  $Q^2$  values available are considered in fitting the *Ansatz* parameters. For illustrative purposes, FRR is performed with a dipole regulator with  $\Lambda = 1.0$  GeV. A direct comparison of the finite-volume-corrected lattice values of  $\langle r^2 \rangle_E$ , using the dipole *Ansatz* from Eq. (30), and the variant *Ansatz* from Eq. (31), is shown in Fig. 7.

In Fig. 5, the estimate of the uncertainty in  $\langle r^2 \rangle_E$  is much smaller than for the other *Ansatz*, raising concerns of an unaccounted for systematic uncertainty. The electric charge radii obtained using the variant *Ansatz* from Eq. (31), as shown in Fig. 6, appear to be the more cautious, in that the error bar encompasses a range of variation from the choice of *Ansatz*. This can be seen most clearly in Fig. 7.

In order to assess the low  $Q^2$  behaviour of the variant *Ansatz* in Eq. (31), a comparison of the  $Q^2$  extrapolation using this *Ansatz* is shown in Fig. 8 at the point:  $m_\pi^2 = 0.50$  GeV<sup>2</sup>. Both  $Q^2$  extrapolations are plotted on the same axes. The lightest three values of  $Q^2$  are used in constraining the parameters. The merit of the extra fit parameter in Eq. (31) is evident.

#### B. Renormalization flow analysis

The QCDSF results for the electric charge radius, displayed in Fig. 1, include a linear extrapolation, which does not take

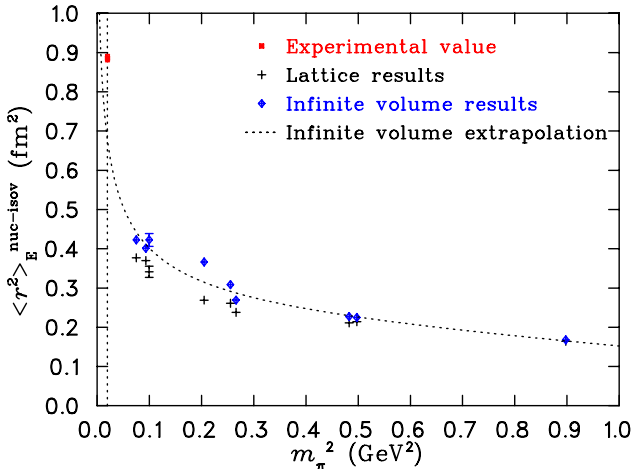


FIG. 5: (color online). Infinite-volume chiral extrapolation of  $\langle r^2 \rangle_E$ , using the dipole  $Q^2$  extrapolation Ansatz from Eq. (30). The infinite-volume corrected lattice points are also shown.

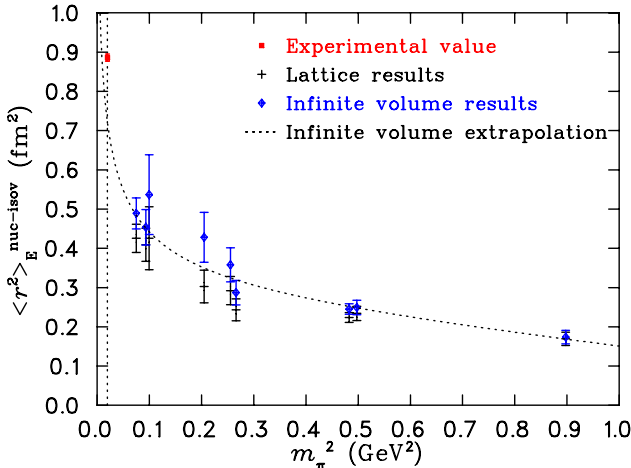


FIG. 6: (color online). Infinite-volume chiral extrapolation of  $\langle r^2 \rangle_E$ , using the variant  $Q^2$  extrapolation Ansatz from Eq. (31).

into account the nonanalytic behaviour of the chiral loop integrals, nor the finite-volume corrections. Neglecting these important effects [37], it is not surprising that the linear trend line does not approach the experimental value of the electric charge radius at the physical pion mass. Since these lattice QCD results extend outside the PCR, the result of an extrapolation will be regularization scale dependent. However, the scale dependence may be constrained using a procedure [18–20] that obtains an optimal regularization scale, and an estimate of its uncertainty, as constrained by the lattice results.

In order to obtain an optimal regularization scale, the low-energy coefficient,  $c_0^{(\mu)}$  from Eq. (29), will be calculated across a range of values of the regularization scale,  $\Lambda$ . Multiple renormalization flow curves may be obtained by constraining the fit window by a maximum value,  $m_{\pi,\max}^2$ , and sequentially adding points to extend further outside the PCR. The renormalization flow curves for a dipole regulator are plotted on the same set of axes in Fig. 9. Within the PCR,  $c_0$  will be insensitive to the value of  $\Lambda$ , and appear as a horizontal line in Fig. 9. In contrast, variation of  $c_0$  with respect to  $\Lambda$  becomes

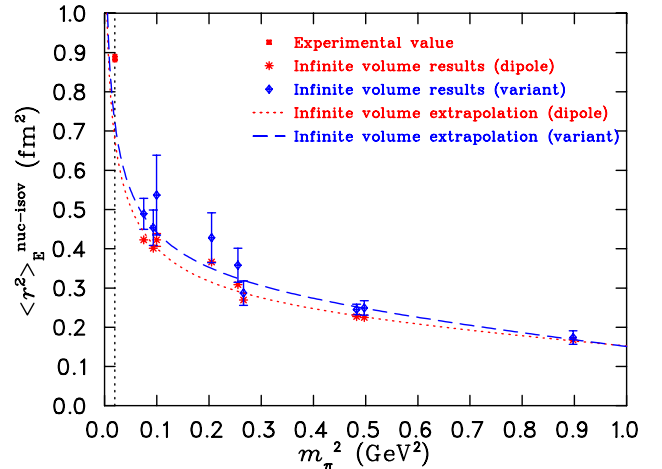


FIG. 7: (color online). A comparison of the infinite-volume chiral extrapolations of  $\langle r^2 \rangle_E$  using the dipole  $Q^2$  extrapolation Ansatz from Eq. (30), and the variant  $Q^2$  extrapolation Ansatz from Eq. (31).

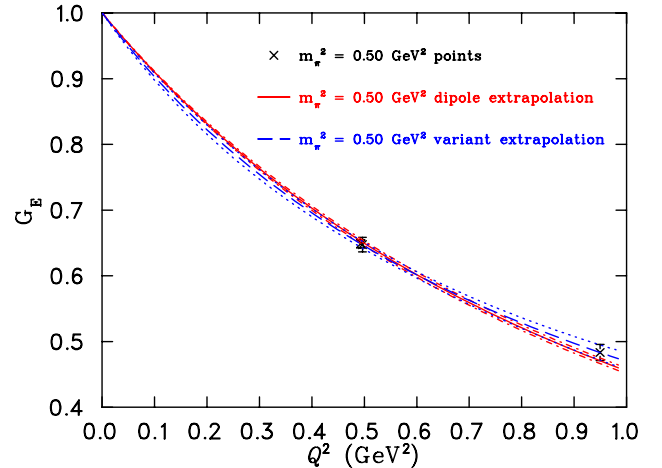


FIG. 8: (color online). A comparison of the  $Q^2$  extrapolation of the electric form factor  $G_E$ , using the normal dipole Ansatz from Eq. (30), and the variant Ansatz, defined in Eq. (31). The smallest three values of  $Q^2$  are used (the smallest two being almost coincident). The fits are shown for  $m_\pi^2 = 0.50$  GeV<sup>2</sup>. Error bands are shown with dotted lines.

larger as one moves further from the PCR. The correct value of  $c_0$ , and thus the optimal value for  $\Lambda$ , is identified by the intersections of the curves, where their deviation is minimal [18].

Unlike the results from the analysis of the nucleon mass [18] or magnetic moment [20], the regularization scale-dependence is relatively weak for  $\Lambda > 0.6$  GeV. There is no distinct intersection point in the renormalization flow curves. This lack of sensitivity to the regularization scale is a consequence of the logarithm in the chiral expansion of Eq. (25), which is slowly-varying with respect to  $\Lambda$ .

An optimal regularization scale for the dipole regulator can be obtained using a  $\chi_{dof}^2$  analysis, taking the degrees of freedom to be the curves of  $c_0$  corresponding to different values of  $m_{\pi,\max}^2$ . For the six different values of  $m_{\pi,\max}^2$  considered in Fig. 9, each curve is described by  $c_0^i(\Lambda)$ , where  $i$  takes values 1 through 6.  $\delta c_0^i(\Lambda)$  denotes the uncertainty in  $c_0^i$  obtained

when fitting the lattice results. The  $\chi_{dof}^2$  for each value of  $\Lambda$  is expressed as

$$\chi_{dof}^2(\Lambda) = \frac{1}{n-1} \sum_{i=1}^n \frac{(c_0^i(\Lambda) - \bar{c}_0(\Lambda))^2}{(\delta c_0^i(\Lambda))^2}, \quad (32)$$

$$\bar{c}_0(\Lambda) = \frac{\sum_{i=1}^n c_0^i(\Lambda) / (\delta c_0^i(\Lambda))^2}{\sum_{j=1}^n 1 / (\delta c_0^j(\Lambda))^2}, \quad (33)$$

with the statistically weighted average  $\bar{c}_0(\Lambda)$  given by Eq. (33). The  $\chi_{dof}^2$  is illustrated in Fig. 10. The value of the optimal scale, obtained using a dipole regulator, is  $\Lambda_{\text{dip}}^{\text{scale}} = 1.08_{-0.32}^{+0.58}$  GeV, which is consistent with the optimal regularization scale values obtained for the nucleon mass using a dipole regulator [18]. The value is also consistent with the result obtained for the nucleon magnetic moment, based on these QCDSF simulations [20]. This provides evidence that, for a given functional form of the regulator, the optimal regularization scale may be associated with an intrinsic scale, characterizing the finite size of the nucleon.

### C. Chiral extrapolations

The identification of an optimal regularization scale allows an accurate chiral extrapolation to be performed. Furthermore, a range of box sizes may be considered, thus providing an estimate of the finite-volume effects. In order to determine the most suitable number of points to be used for fitting the lattice results, the method described in Refs. [19, 20] is used.

In extrapolating the electric charge radius, the statistical uncertainty comprises contributions from the fit coefficients. In the case of the systematic uncertainty, the axial coupling and the pion decay constant are assumed to be sufficiently well-determined experimentally. Thus, the dominant contribution to the systematic uncertainty in the extrapolation is associated with the optimal regularization scale.

A second source of systematic uncertainty is due to the choice of the regulator functional form, which is combined in quadrature,

$$\left(\delta\langle r^2 \rangle_E^{\text{sys}}\right)^2 = \left(\delta\langle r^2 \rangle_E^{\Lambda}\right)^2 + \left(\delta\langle r^2 \rangle_E^{\text{reg}}\right)^2. \quad (34)$$

$\delta\langle r^2 \rangle_E^{\text{reg}}$  is obtained by comparing the result of a dipole regulator to that of using a sharp cutoff, which has an intrinsic scale of  $\Lambda_{\text{sc}}^{\text{scale}} = 0.51_{-0.10}^{+0.17}$  GeV, determined using the same methods described for the dipole regulator. The systematic uncertainty is taken as half the difference between the central values of each case. Though the sharp cutoff regulator does not provide higher-order nonanalytic contributions in the chiral expansion [38] and is less physical than the dipole regulator, a comparison between the two regulators provides the most cautious evaluation of the dependence of the result on the functional form of the regulator.

The value of the extrapolation of  $\langle r^2 \rangle_E$  to the physical point is shown in Fig. 11 for different values of  $m_{\pi, \text{max}}^2$ . Statistical and systematic errors have been added in quadrature. Fig. 12 shows the magnitude of the statistical and systematic error

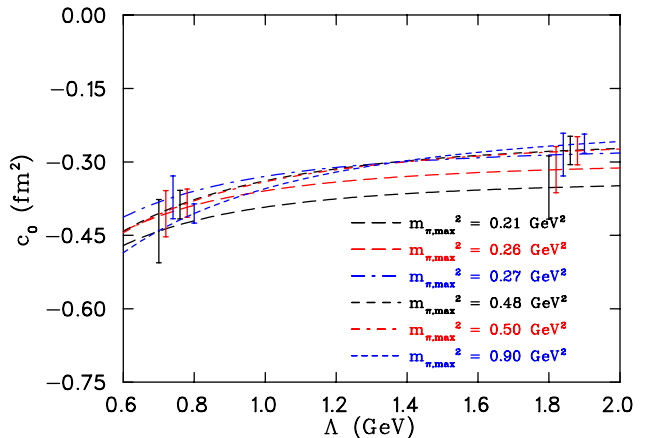


FIG. 9: (color online). The renormalization flow of  $c_0^{(\mu)}$ , obtained using a dipole regulator, and based on QCDSF simulation results.  $c_0^{(\mu)}$  is calculated relative to the mass scale,  $\mu = 1$  GeV. For each curve, two arbitrary values of  $\Lambda$  are chosen to indicate the general size of the error bars.

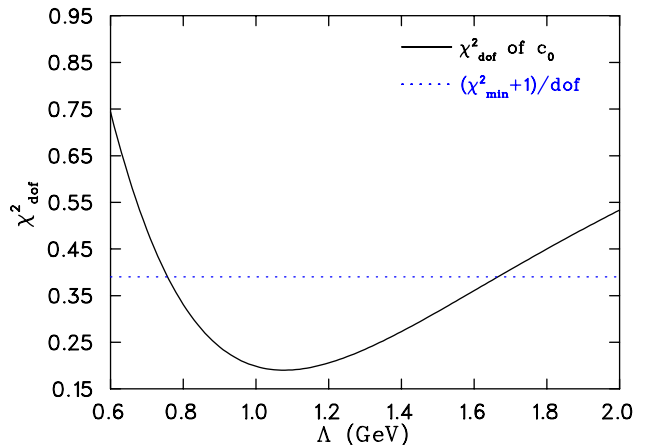


FIG. 10: (color online). A  $\chi_{dof}^2$  analysis for the renormalization flow of  $c_0^{(\mu)}$ , obtained using a dipole regulator, and based on QCDSF simulation results. The dotted line illustrates the upper limit:  $(\chi_{\text{min}}^2 + 1)/dof$ .

bars separately, in addition to the total uncertainty. These plots allow the identification of the optimal number of lattice results to be used for an extrapolation, which is signified by the best compromise between the statistical and the systematic uncertainties. Figure 12 indicates that, in this case, the lightest seven lattice points should be used, corresponding to a value of  $m_{\pi, \text{max}}^2 \simeq 0.48$  GeV<sup>2</sup>. Table I summarizes the breakdown of each error bar into its source components.

Note that there is a discrepancy between the experimental value and the extrapolation results. This could be a consequence of excited state contamination in the lattice calculation of the three-point function; the use of only two flavours, and/or neglecting  $\mathcal{O}(a)$  effects.

### D. Finite-volume effects in future lattice simulations

To predict the finite-volume dependence of future lattice simulations, consider again the electric charge radii from the lattice, corrected to infinite volume obtained using the variant

TABLE I: Results for the isovector nucleon electric charge radius, extrapolated to the physical point using different values of  $m_{\pi,\max}^2$ , as illustrated in Fig. 11. The uncertainty in  $\langle r^2 \rangle_E(m_{\pi,\text{phys}}^2)$  is provided in the following order: the statistical uncertainty, the uncertainty due to  $\Lambda^{\text{scale}}$ , the uncertainty due to the change in regulator functional form, and the total uncertainty, respectively. The value of  $\Lambda^{\text{scale}}$  is calculated for each choice of regulator functional form.

$m_{\pi,\max}^2(\text{GeV}^2)$	$\langle r^2 \rangle_E(m_{\pi,\text{phys}}^2)$ (fm <sup>2</sup> )	$\delta\langle r^2 \rangle_E^{\text{stat}}$	$\delta\langle r^2 \rangle_E^{\Lambda}$	$\delta\langle r^2 \rangle_E^{\text{reg}}$	$\delta\langle r^2 \rangle_E^{\text{tot}}$
0.205	0.705	0.055	0.017	0.006	0.058
0.255	0.731	0.042	0.019	0.007	0.047
0.266	0.755	0.040	0.020	0.007	0.045
0.483	0.753	0.028	0.031	0.008	0.043
0.497	0.751	0.028	0.032	0.008	0.043
0.898	0.746	0.019	0.051	0.007	0.055

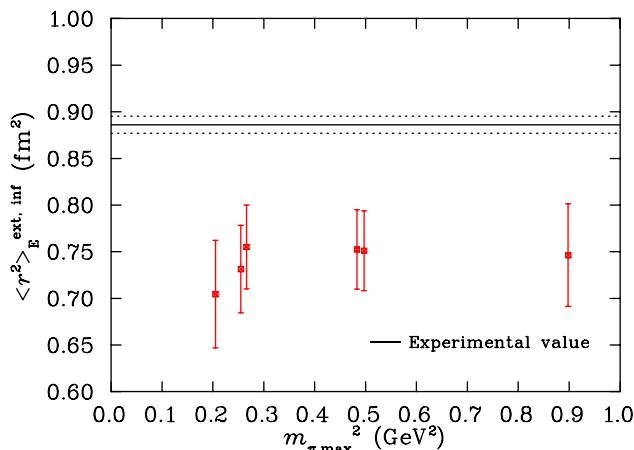


FIG. 11: (color online). Behaviour of the extrapolation of  $\langle r^2 \rangle_E$  to the physical point, vs.  $m_{\pi,\max}^2$ . The value of  $\Lambda^{\text{scale}}$  is used, as obtained from the  $\chi_{dof}^2$  analysis. The error bars include the statistical and systematic uncertainties added in quadrature.

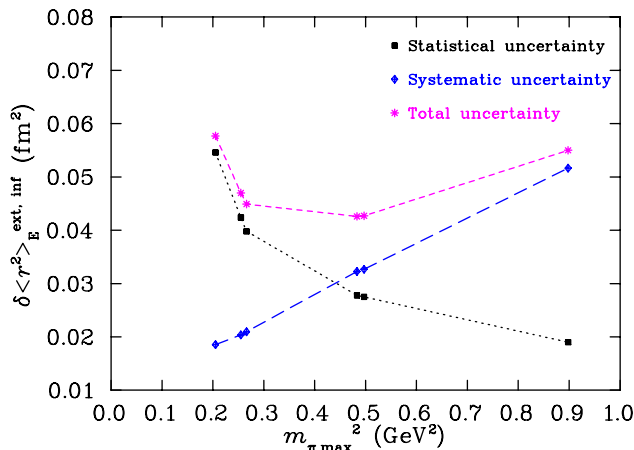


FIG. 12: (color online). Magnitude of the statistical, systematic and total error bars in the extrapolation of  $\langle r^2 \rangle_E$  to the physical point, vs.  $m_{\pi,\max}^2$ . In each case of regulator, the value of  $\Lambda^{\text{scale}}$  is used, as obtained from the corresponding  $\chi_{dof}^2$  analysis. At a maximum pion mass of  $\hat{m}_{\pi,\max}^2 = 0.48$  GeV<sup>2</sup>, the best compromise between statistical and systematic uncertainty is achieved.

*Ansatz* defined in Eq. (31). As shown in Fig. 13, this time the experimental value is included in the fit, and the chiral extrapolation at infinite volume is shown.

With the fit parameters determined, extrapolations at a variety of finite volumes are shown in Fig. 14. The extrapolations use the lightest seven data points, and are only calculated for values  $m_{\pi}L > 3$ , as in the initial selection of the lattice simulation results. These finite-volume results allow comparisons with current lattice simulations, and also allow estimates of finite-volume effects at arbitrary box sizes to be made. For example, using a box size of  $L \sim 4$  fm, a significant deviation from the infinite-volume limit is observed. In this case, the finite-volume radius is  $\langle r^2 \rangle_E^{\text{nuc-isov}} = 0.745$  fm; significantly below the physical value of 0.886 fm used to constrain the fit.

In addition, the finite-volume extrapolations can provide a benchmark for lattice QCD simulations at large and currently untested box sizes. The extrapolation curves indicate that a box length of  $L \gtrsim 7$  fm is required to achieve an extrapolation within 2% of the infinite-volume result.

This extrapolation method may be used to provide specific predictions for the charge radius based on lattice configurations from the PACS-CS Collaboration [39], freely available via the International Lattice Data Grid (ILDG). By choosing the lattice volume and the  $m_{\pi}^2$  values to match the PACS-CS data, an estimate of the expected charge radii to be observed in future lattice simulations are shown in Fig. 15. It is noteworthy that the predicted values of the charge radius near the physical point do not approach the experimental point at the PACS-CS lattice volume of  $L = 2.9$  fm. This emphasizes the importance of using  $\chi$ EFT to correct for finite-volume effects, until very large lattice volumes can be used to resolve the correct chiral nonanalytic behaviour of hadrons.

#### IV. CONCLUSION

Newly developed techniques within the framework of chiral effective field theory were applied to recent precision lattice QCD results from the QCDSF Collaboration for the charge radius of the isovector nucleon. The inclusion of chiral loop contributions is vital for reconciling lattice simulations with the experimental result. It was discovered that the logarithmic divergence in the chiral expansion of the charge radius drives

the large finite-volume corrections encountered near the physical point. Lattice box sizes of  $L \gtrsim 7$  fm are required in order to achieve a direct lattice simulation result within 2% of the value at the physical point.

A discrepancy was found between the experimental value and the extrapolation results, which may be a consequence of excited state contamination; the use of only two flavours, and/or neglecting  $\mathcal{O}(a)$  contributions.

Finite-volume chiral extrapolations provide a benchmark for future lattice simulations. Specific predictions can be made by choosing lattice volumes and pion masses to match

those of a lattice calculation. By using this method, estimates of the electric charge radii simulations were obtained based on the PACS-CS configurations, which provide a guide for the interpretation of future lattice results.

### Acknowledgments

We would like to thank James Zanotti for many helpful discussions. This research is supported by the Australian Research Council through Grants No. DP110101265 and No. FT120100821 (R.D.Y.).

- 
- [1] H.-y. Gao, *Int.J.Mod.Phys.* **E12**, 1 (2003), nucl-ex/0301002.
  - [2] C. E. Hyde and K. de Jager, *Ann.Rev.Nucl.Part.Sci.* **54**, 217 (2004), nucl-ex/0507001.
  - [3] J. Arrington, C. Roberts, and J. Zanotti, *J.Phys.G* **G34**, S23 (2007), nucl-th/0611050.
  - [4] C. Perdrisat, V. Punjabi, and M. Vanderhaeghen, *Prog.Part.Nucl.Phys.* **59**, 694 (2007), hep-ph/0612014.
  - [5] J. Arrington, K. de Jager, and C. F. Perdrisat, *J.Phys.Conf.Ser.* **299**, 012002 (2011), 1102.2463.
  - [6] T. Yamazaki, Y. Aoki, T. Blum, H.-W. Lin, S. Ohta, et al., *Phys.Rev.* **D79**, 114505 (2009), 0904.2039.
  - [7] S. Syritsyn, J. Bratt, M. Lin, H. Meyer, J. Negele, et al., *Phys.Rev.* **D81**, 034507 (2010), 0907.4194.
  - [8] J. Bratt et al. (LHPC Collaboration), *Phys.Rev.* **D82**, 094502 (2010), 1001.3620.
  - [9] C. Alexandrou, M. Brinet, J. Carbonell, M. Constantinou, P. Harraud, et al., *Phys.Rev.* **D83**, 094502 (2011), 1102.2208.
  - [10] S. Collins, M. Gockeler, P. Hagler, R. Horsley, Y. Nakamura, et al., *Phys.Rev.* **D84**, 074507 (2011), 1106.3580.
  - [11] B. C. Tiburzi, *Phys.Rev.* **D77**, 014510 (2008), 0710.3577.
  - [12] J. Hu, F.-J. Jiang, and B. C. Tiburzi, *Phys.Lett.* **B653**, 350 (2007), 0706.3408.
  - [13] F.-J. Jiang and B. Tiburzi, *Phys.Rev.* **D78**, 114505 (2008), 0810.1495.
  - [14] J. Hall, D. Leinweber, B. Owen, and R. Young (2012), 1210.6124.
  - [15] D. B. Leinweber, A. W. Thomas, and R. D. Young, *Phys.Rev.Lett.* **92**, 242002 (2004), hep-lat/0302020.
  - [16] D. B. Leinweber, A. W. Thomas, and R. D. Young, *PoS LAT2005*, 048 (2006), hep-lat/0510070.
  - [17] D. B. Leinweber, A. W. Thomas, and R. D. Young, *Nucl. Phys.* **A755**, 59 (2005), hep-lat/0501028.
  - [18] J. M. M. Hall, D. B. Leinweber, and R. D. Young, *Phys. Rev.* **D82**, 034010 (2010), 1002.4924.
  - [19] J. Hall, F. Lee, D. Leinweber, K. Liu, N. Mathur, et al., *Phys.Rev.* **D84**, 114011 (2011), 1101.4411.
  - [20] J. Hall, D. Leinweber, and R. Young, *Phys.Rev.* **D85**, 094502 (2012), 1201.6114.
  - [21] C. Aubin, C. Bernard, C. DeTar, J. Osborn, S. Gottlieb, et al., *Phys.Rev.* **D70**, 094505 (2004), hep-lat/0402030.
  - [22] P. J. Mohr, B. N. Taylor, and D. B. Newell, *Rev.Mod.Phys.* **84**, 1527 (2012), 1203.5425.
  - [23] J. Beringer et al. (Particle Data Group), *Phys.Rev.* **D86**, 010001 (2012).
  - [24] E. E. Jenkins and A. V. Manohar, *Phys. Lett.* **B255**, 558 (1991).
  - [25] E. E. Jenkins, *Nucl. Phys.* **B368**, 190 (1992).
  - [26] E. E. Jenkins and A. V. Manohar (1991), talk presented at the Workshop on Effective Field Theories of the Standard Model, Dobogoko, Hungary, Aug 1991.
  - [27] J. N. Labrenz and S. R. Sharpe, *Phys. Rev.* **D54**, 4595 (1996), hep-lat/9605034.
  - [28] A. Walker-Loud, *Nucl. Phys.* **A747**, 476 (2005), hep-lat/0405007.
  - [29] P. Wang, D. B. Leinweber, A. W. Thomas, and R. D. Young, *Phys. Rev.* **D75**, 073012 (2007), hep-ph/0701082.
  - [30] R. F. Lebed, *Phys. Rev.* **D51**, 5039 (1995), hep-ph/9411204.
  - [31] W. Armour, C. R. Allton, D. B. Leinweber, A. W. Thomas, and R. D. Young, *J. Phys.* **G32**, 971 (2006), hep-lat/0510078.
  - [32] S. R. Beane, *Phys. Rev.* **D70**, 034507 (2004), hep-lat/0403015.
  - [33] A. Ali Khan et al. (QCDSF-UKQCD), *Nucl. Phys.* **B689**, 175 (2004), hep-lat/0312030.
  - [34] M. Gell-Mann, R. J. Oakes, and B. Renner, *Phys. Rev.* **175**, 2195 (1968).
  - [35] R. D. Young, D. B. Leinweber, and A. W. Thomas, *Prog.Part.Nucl.Phys.* **50**, 399 (2003), hep-lat/0212031.
  - [36] J. Kelly, *Phys.Rev.* **C70**, 068202 (2004).
  - [37] D. B. Leinweber and T. D. Cohen, *Phys.Rev.* **D47**, 2147 (1993), hep-lat/9211058.
  - [38] D. Djukanovic, M. R. Schindler, J. Gegelia, and S. Scherer, *Phys. Rev.* **D72**, 045002 (2005), hep-ph/0407170.
  - [39] S. Aoki et al. (PACS-CS Collaboration), *Phys.Rev.* **D79**, 034503 (2009), 0807.1661.



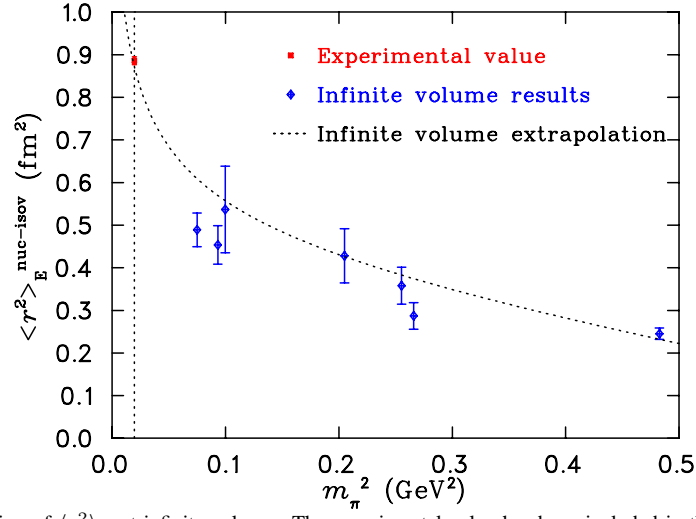


FIG. 13: (color online). Extrapolation of  $\langle r^2 \rangle_E$  at infinite volume. The experimental value has been included in the fit, in preparation for making future finite-volume corrections.

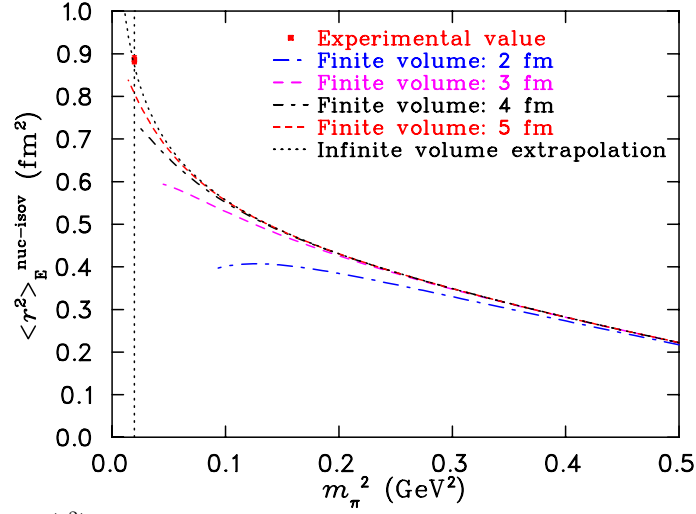


FIG. 14: (color online). Extrapolations of  $\langle r^2 \rangle_E$  at different finite volumes, and at infinite volume. The curves are based on lattice QCD results from QCDSF, lattice sizes: 1.7 – 2.9 fm, and the experimental value. The provisional constraint  $m_\pi L > 3$  is used. The experimental value [22, 23] is marked as a square.

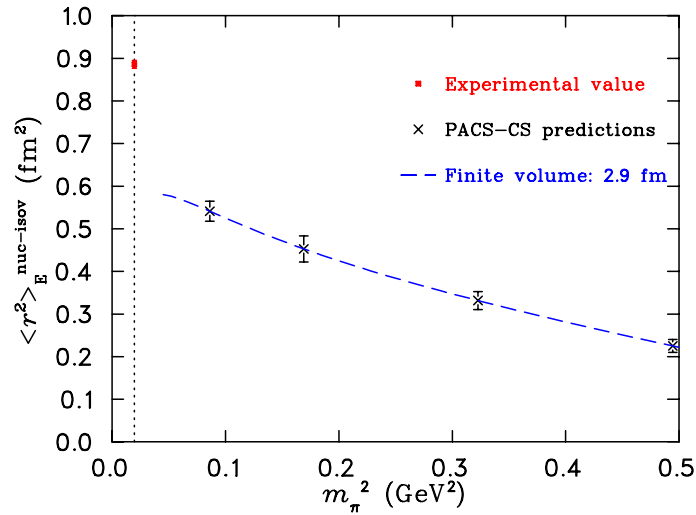


FIG. 15: (color online). Predictions of  $\langle r^2 \rangle_E$  based on the volume ( $L = 2.9$  fm) and pion masses from the PACS-CS lattice QCD configurations [39]. The error bars represent the total uncertainties. The points are estimated only within the constraint  $m_\pi L > 3$ .